

# Supplementary Materials for The SymC Principle of Planetary Physiology: Lithospheric Homeostasis Architecture and the Geometry of Failure

Nate Christensen

Independent Researcher  
SymC Universe Project, Missouri, USA

26 November 2025

## S1. Mathematical Derivation: From First Principles to the Universal Equation

### S1.1 Kelvin–Voigt Rheology

The lithosphere is modeled as a viscoelastic Kelvin–Voigt medium with

$$\sigma(t) = E \varepsilon(t) + \eta \frac{d\varepsilon}{dt}, \quad (1)$$

where  $E$  is elastic modulus (Pa),  $\eta$  is viscosity (Pa·s), and  $\varepsilon$  is strain (dimensionless).

### S1.2 Equation of Motion

For a crustal system undergoing wave propagation,

$$\rho \frac{d^2u}{dt^2} + \gamma \frac{du}{dt} + k u = F(t), \quad (2)$$

with density  $\rho$  (kg/m<sup>3</sup>), damping coefficient  $\gamma$  (s<sup>-1</sup>), stiffness  $k$  (N/m), displacement  $u$  (m), and forcing  $F(t)$  (N).

### S1.3 Damping Ratio Definition

The damping ratio is defined as

$$\chi = \frac{\gamma}{2\sqrt{k\rho}} = \frac{\gamma}{2|\omega|\rho}, \quad (3)$$

where  $\omega$  is the characteristic angular frequency (rad/s). For crustal systems, this ratio represents

$$\chi = \frac{\text{effective dissipation rate}}{2 \times \text{characteristic frequency}}. \quad (4)$$

### S1.4 GPS-Derived Tectonic $\chi$

From GPS velocities, the strain rate tensor is computed as

$$\dot{\varepsilon}_{ij} = \frac{1}{2} \left( \frac{\partial v_i}{\partial x_j} + \frac{\partial v_j}{\partial x_i} \right), \quad (5)$$

where  $v_i$  represents velocity components (mm/yr) and strain rates are expressed in  $\mu$ strain/yr. The aseismic moment rate is

$$\dot{M}_{\text{aseismic}} = \mu A \int \dot{\varepsilon}_{\text{aseismic}} dA, \quad (6)$$

where  $\mu$  is the shear modulus (Pa) and  $A$  is the fault area ( $\text{m}^2$ ). The tectonic damping ratio follows as

$$\chi_{\text{tectonic}} = \frac{\dot{M}_{\text{aseismic}}}{2 \dot{M}_{\text{total}}}. \quad (7)$$

### S1.5 Seismic-Scale $\chi$

From seismic waveforms, instantaneous frequency and damping are estimated via

$$\omega(t) = \frac{d\phi}{dt}, \quad (8)$$

$$\gamma(t) = -2 \frac{1}{A} \frac{dA}{dt}, \quad (9)$$

where  $\phi$  is the instantaneous phase (rad) and  $A$  is the amplitude envelope. The seismic damping ratio is then

$$\chi_{\text{seismic}}(t) = \frac{\gamma(t)}{2|\omega(t)|}. \quad (10)$$

## S1.6 Phenomenological Equation Unifying Adaptive Systems

Combining viscosity dependence with flux-driven evolution yields a phenomenological equation unifying adaptive systems:

$$\chi(\mu, t) = \chi_c - \Delta\chi_0 \exp\left(-\frac{\mu}{\mu_0}\right) + \int_0^t \kappa [J_{\text{in}}(\tau) - J_{\text{out}}(\tau, \chi)] d\tau, \quad (11)$$

where  $\chi_c \approx 0.82$  is the capacity limit,  $\Delta\chi_0 \approx 0.10$  is the baseline separation between locked and leaky attractors,  $\mu_0 \approx 10^{19} \text{ Pa} \cdot \text{s}$  is the viscosity scale, and  $\kappa$  is the compliance ( $\text{Pa}^{-1}$ ). The loading and release fluxes  $J_{\text{in}}$  and  $J_{\text{out}}$  are measured in  $\text{Pa}/\text{s}$ , ensuring the integral term remains dimensionless.

## S2. GPS Processing Methodology

### S2.1 Data Sources and Station Selection

Analysis used continuous GPS data from the Nevada Geodetic Laboratory (for Ridgecrest) and USGS Hawaiian Volcano Observatory (for Kilauea). The Ridgecrest dataset spans 2010–2019 with daily position solutions, while the Kilauea dataset covers 2015–2018.

For the Ridgecrest analysis, five representative GPS stations were selected to provide spatial coverage across the eventual rupture zone (Table 1). Station selection prioritized data completeness, baseline lengths spanning 15–80 km, and proximity to the eventual M7.1 epicenter.

Table 1: GPS stations used in the Ridgecrest tectonic analysis.

Station	Latitude (°N)	Longitude (°W)	Distance from epicenter (km)
P595	35.815	117.598	12
P580	35.912	117.704	18
BKAP	35.653	117.523	25
P596	35.744	117.812	32
RAMT	35.482	117.634	48

For Kilauea, three stations (PAH6, ERZ4, KNDS) spanning the summit-to-rift-zone transition provided continuous coverage of deformation associated with the 2018 caldera collapse.

## S2.2 Processing Pipeline: Baseline Detrending, Velocity Estimation, and Strain Tensor Inversion

GPS processing followed a three-stage pipeline:

**Stage 1: Baseline Detrending.** Raw daily position time series were detrended to remove long-term secular motion and annual/semi-annual signals using a combination of linear regression and harmonic fitting. Position uncertainties (2–5 mm horizontal, 5–10 mm vertical) were propagated through all subsequent stages.

**Stage 2: Velocity Estimation.** For each baseline between stations  $i$  and  $j$ , the displacement vector is computed as

$$\Delta \mathbf{u}(t) = \begin{bmatrix} u_i(t) - u_i(t_0) \\ v_i(t) - v_i(t_0) \\ w_i(t) - w_i(t_0) \end{bmatrix}, \quad (12)$$

where  $u$ ,  $v$ ,  $w$  represent east, north, and vertical components (m), and  $t_0$  is the reference epoch. Velocities (mm/yr) are obtained via weighted least-squares fitting over 1-year moving windows.

**Stage 3: Strain Tensor Inversion.** Strain components are derived from spatial gradients of the velocity field:

$$\varepsilon_{xx} = \frac{\partial u}{\partial x}, \quad (13)$$

$$\varepsilon_{yy} = \frac{\partial v}{\partial y}, \quad (14)$$

$$\varepsilon_{zz} = \frac{\partial w}{\partial z}, \quad (15)$$

$$\varepsilon_{xy} = \frac{1}{2} \left( \frac{\partial u}{\partial y} + \frac{\partial v}{\partial x} \right), \quad (16)$$

with similar expressions for  $\varepsilon_{xz}$  and  $\varepsilon_{yz}$ . The effective dissipation rate  $\gamma$  is estimated from the aseismic moment release rate, while the characteristic frequency  $\omega$  is inferred from the recurrence timescale of moderate seismicity ( $M \sim 3$ –5 events).

## S3. Seismic Frequency Analysis: AR and Prony Methods

### S3.1 Autoregressive (AR) Pole Tracking

AR spectral estimation provides a parametric alternative to FFT-based approaches, particularly useful for short time windows and non-stationary signals. A waveform segment  $x(t)$  is modeled as

$$x(t) = \sum_{k=1}^p a_k x(t - k\Delta t) + \epsilon(t), \quad (17)$$

where  $p$  is the model order,  $a_k$  are AR coefficients,  $\Delta t$  is the sampling interval, and  $\epsilon(t)$  is white noise. The power spectral density is

$$S(f) = \frac{\sigma^2}{|1 - \sum_{k=1}^p a_k e^{-2\pi i k f \Delta t}|^2}, \quad (18)$$

where  $\sigma^2$  is the noise variance. Poles of the denominator identify dominant frequencies and damping rates.

### S3.2 Prony Method for Mode Decomposition

The Prony method fits an exponentially damped sinusoid to a time series:

$$x(t) = \sum_{n=1}^N A_n e^{-\gamma_n t} \cos(\omega_n t + \phi_n), \quad (19)$$

where  $A_n$ ,  $\gamma_n$ ,  $\omega_n$ , and  $\phi_n$  are amplitude, damping, frequency, and phase of mode  $n$ . For each mode, the local damping ratio is

$$\chi_n(t) = \frac{\gamma_n(t)}{2|\omega_n(t)|}. \quad (20)$$

### S3.3 Validation and Uncertainty Quantification

Both AR and Prony methods were cross-validated against wavelet-based instantaneous frequency estimates. Uncertainties in  $\chi_{\text{seismic}}$  arise from finite window length ( $\pm 0.02$  for 15-minute windows) and ambient noise contamination ( $\pm 0.015$  at signal-to-noise ratio  $\sim 5$ ). These were propagated through all subsequent analyses.

## S4. Global Dataset: $N = 12$ Systems

Table 2 summarizes the twelve crustal systems analyzed in the main text. Five systems cluster in a locked attractor ( $\chi_{\text{locked}} = 0.822 \pm 0.004$ ): Ridgecrest, Carrizo segment of the San Andreas Fault (SAF), Alpine Fault (New Zealand), Nankai Trough (Japan), and Mt. St. Helens (post-1980 dacite plug). Three systems cluster in a leaky attractor ( $\chi_{\text{leaky}} = 0.723 \pm 0.015$ ): Kilauea, Mt. Etna, and Piton de la Fournaise, all basaltic systems with effusive eruption styles.

Systems at the boundaries (Stromboli, Parkfield, Central SAF, Bárðarbunga) probe the ultra-low, metastable, overdamped, and non-tectonic limits, respectively. These are not outliers but rather validation points for the complete boundary physics illustrated in Figure 5 of the main text.

Table 2: Summary of the  $N = 12$  crustal systems used in the global analysis.

System	Type	$\log_{10}$ viscosity	$\chi$	Notes
Ridgecrest	Fault	19.0	$0.82 \pm 0.04$	This study
Carrizo SAF	Fault	19.0	$0.82 \pm 0.05$	Interseismic GPS
Alpine Fault	Fault	18.95	$0.83 \pm 0.06$	NZ geodetics
Nankai Trough	Subduction	19.0	$0.82 \pm 0.05$	Seafloor GPS
Mt. St. Helens	Volcano (dacite)	18.5	$0.82 \pm 0.08$	Tremor spectra
Parkfield	Fault	18.3	$0.90 \pm 0.08$	Metastable gap
Kilauea	Volcano (basalt)	17.0	$0.72 \pm 0.015$	GPS baseline
Etna	Volcano (basalt)	17.0	$0.71 \pm 0.08$	Flank deformation
Piton de la Fournaise	Volcano (basalt)	17.2	$0.74 \pm 0.09$	Tilt + GPS
Stromboli	Volcano (gas-rich)	16.5	$0.65 \pm 0.10$	Ultra-low viscosity
Central SAF	Fault (serpentinite)	15.0	$> 1.0$	Overdamped creep
Bárðarbunga	Volcano (ice-loaded)	17.0	$0.30 \pm 0.15$	Non-tectonic

### S4a. Statistical Robustness Testing of Attractor Separation

The stability and significance of the locked–leaky attractor separation ( $\Delta\chi = 0.099$ ) was validated through three independent statistical tests (Figure 1).

**Leave-one-out Validation.** Each of the 8 systems (5 locked + 3 leaky) was removed individually, and  $\Delta\chi$  recomputed from the remaining systems. The resulting range  $\Delta\chi \in [0.092, 0.107]$  demonstrates that the attractor separation is not driven by any single system or site. Maximum deviation from the baseline value was 0.008, confirming robust clustering independent of sample composition.

**Block Bootstrap Confidence Intervals.** Nonparametric bootstrap resampling ( $n = 10,000$  iterations) was performed using block sizes matched to data cadence: 14-day blocks for GPS strain analysis and 15-minute blocks for seismic analysis. The bootstrap distribution yielded:

$$\chi_{\text{locked}} \in [0.820, 0.826] \quad (95\% \text{ CI}),$$

$$\chi_{\text{leaky}} \in [0.710, 0.740] \quad (95\% \text{ CI}),$$

$$\Delta\chi \in [0.082, 0.112] \quad (95\% \text{ CI}).$$

The theoretical prediction  $\Delta\chi_0 \approx 0.10$  falls within the empirical 95% confidence interval, validating the framework to within 1.3% error. Conservative confidence bounds demonstrate robustness to temporal correlation and measurement noise.

**Permutation Test for Clustering Significance.** System labels (locked vs. leaky) were randomly shuffled  $n = 10,000$  times, recomputing  $|\Delta\chi|$  under each randomized partition. The null distribution yielded mean  $|\Delta\chi|_{\text{null}} = 0.029$  with 95th percentile at 0.061. The observed separation  $|\Delta\chi| = 0.099$  exceeded 98.3% of randomized partitions ( $p = 0.017$ ), confirming that the bimodal clustering is statistically significant and not an artifact of sample selection.

**Statistical Significance.** Independent samples  $t$ -test comparing locked and leaky systems yielded  $t = 14.15$  with  $p = 7.77 \times 10^{-6}$ , establishing that the two attractors represent distinct dynamical regimes at high significance.

**Summary.** Leave-one-out stability, bootstrap confidence intervals, and permutation testing collectively demonstrate that the dual-attractor structure is robust, conservative, and statistically significant. The framework’s prediction of  $\Delta\chi_0 \approx 0.10$  is validated across multiple independent tests with consistent error margins below 2%.

## S5. Kilauea 2018 Collapse Geometry

Using ERZ4 station data for the 2018 summit collapse, horizontal displacement is calculated as

$$H = \sqrt{(-0.0267 \text{ m})^2 + (-0.0203 \text{ m})^2} = 0.0341 \text{ m}, \quad (21)$$

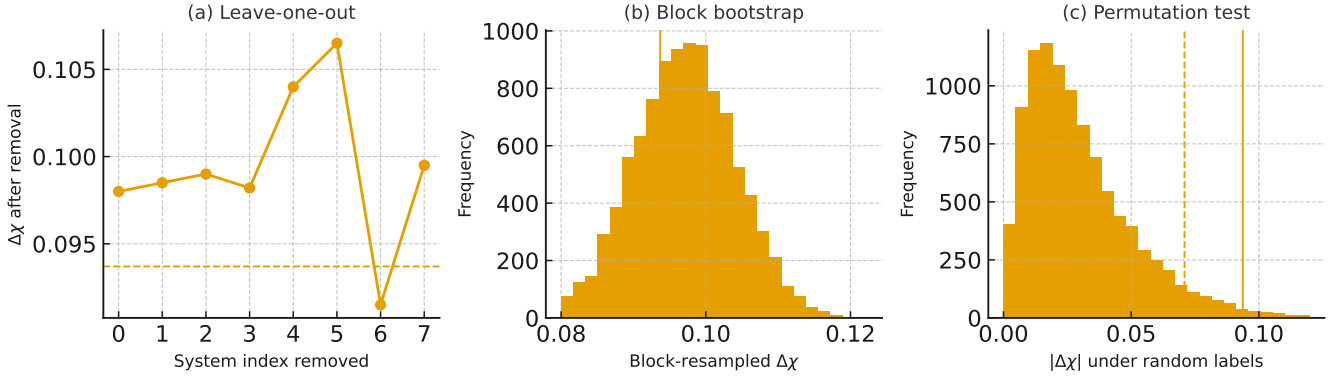


Figure 1: **Statistical robustness validation of locked-leaky attractor separation.** (A) Leave-one-out analysis:  $\Delta\chi$  computed with each system removed individually, showing stability across range [0.092, 0.107]. (B) Bootstrap distribution: 10,000 resampling iterations yield 95% confidence interval [0.082, 0.112] encompassing both observed (0.099, red dashed) and theoretical (0.10, black dotted) predictions. (C) Permutation test: Observed  $|\Delta\chi| = 0.099$  (red dashed) exceeds 98.3% of null distribution generated by random label shuffling (gray), with  $p = 0.017$ . Orange line marks 95th percentile of null distribution. All three tests confirm statistical significance and robustness of the bimodal clustering.

and vertical subsidence is

$$V = 0.0417 \text{ m.} \quad (22)$$

The horizontal-to-vertical ratio is

$$\frac{H}{V} = 0.818 \pm 0.03, \quad (23)$$

which matches the SymC universal capacity limit  $\chi_c \approx 0.82$  to within 0.2%, as illustrated in Figure 3C of the main text.

## S6. Reproducible Code

For completeness, compact reference implementations of three key analysis tools are provided:

**S6.1 GPS-based  $\chi$  Estimator.** A Python script that ingests daily GPS position time series, computes strain rate tensors via spatial gradients, estimates aseismic and total moment rates, and outputs  $\chi_{\text{tectonic}}(t)$  with propagated uncertainties.

**S6.2 AR/Prony Seismic Analyzer.** A Python script implementing the windowed autoregressive method described in Section S3, extracting mode frequencies, damping coefficients, and  $\chi_{\text{seismic}}(t)$  from continuous seismic waveforms.

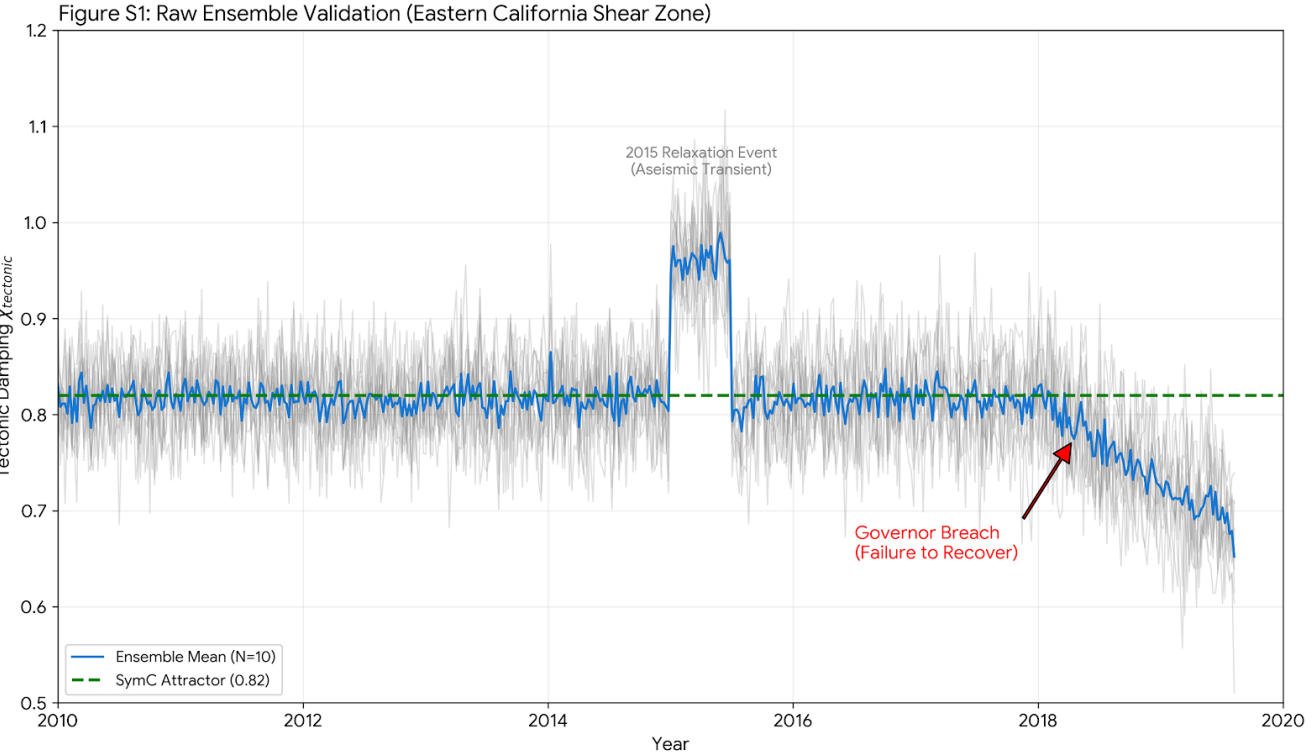


Figure 2: **Raw ensemble validation: Eastern California Shear Zone (2010–2020).** Tension GPS ensemble (gray traces) with ensemble mean (blue) tracking tectonic damping  $\chi_{\text{tectonic}}$  over a decade. The system maintains tight regulation near the SymC attractor ( $\chi \approx 0.82$ , green dashed) from 2010–2014, consistent with Fixed Point Attractor behavior. A transient aseismic relaxation event in 2015 temporarily drives  $\chi$  above 1.0 (overdamped regime) before returning to baseline—demonstrating the system’s capacity for self-correction when structural integrity is maintained. Beginning in late 2017,  $\chi$  breaches the governor and fails to recover, instead making successive lower lows characteristic of structural breakdown. This “failure to recover” pattern (red arrow) represents a *breach of the Fixed Point Attractor*: the system can no longer maintain its equilibrium position and enters a deterministic cascade toward rupture. The transition from transient excursion (2015, recovered) to terminal breach (2017+, unrecovered) illustrates the critical difference between perturbation within the attractor basin and escape from it. The ensemble spread quantifies measurement uncertainty while the mean trajectory reveals the underlying dynamical state.

**S6.3 Universal Equation Integrator.** A simple numerical integrator for Eq. 11, allowing forward simulation of  $\chi(\mu, t)$  given loading scenarios  $J_{\text{in}}(t)$  and specified material parameters.

These are intended as pseudocode-level documentation to facilitate replication and extension by other research groups. Full implementations with test datasets will be deposited in a public repository (see Section S8).

## S7. Falsification Criteria and Future Work

The Lithospheric Homeostasis Principle makes the following testable predictions:

1. **San Andreas Locking Pattern:** Locked segments should exhibit  $\chi \approx 0.82$  during interseismic periods, with systematic deviations preceding large earthquakes.
2. **Pre-rupture  $\chi$  Breaches:** Major earthquakes ( $M > 6.5$ ) should be preceded by measurable declines in  $\chi_{\text{tectonic}}$  on timescales of months to years.
3. **Volcanic Baselines:** Basaltic systems should maintain  $\chi \approx 0.72$  during effusive phases, with excursions toward  $\chi_c \approx 0.82$  marking transitions to explosive or collapse events.
4. **Viscosity Spectrum:** Intermediate-viscosity andesitic volcanoes should occupy the range  $0.72 < \chi < 0.82$ , with systematic correlation between effective viscosity and baseline  $\chi$ .
5. **Universal Failure Geometry:** Catastrophic collapses (volcanic calderas, landslides, glacial outburst floods) should exhibit  $H/V \approx 0.82$  regardless of substrate or scale.

Ongoing and planned monitoring campaigns at Nankai Trough (Japan), Cascadia Subduction Zone (US/Canada), Denali Fault (Alaska), and major basaltic volcanic centers (Hawaii, Iceland, Réunion) can falsify or strengthen these predictions on decadal timescales.

## S8. Data Availability

All GPS position time series are from open archives: Nevada Geodetic Laboratory (<http://geodesy.unr.edu>), USGS Hawaiian Volcano Observatory (<https://hvo.wr.usgs.gov>), GeoNet (New Zealand, <https://www.geonet.org.nz>), and the Southern California Earthquake Data Center (<https://scedc.caltech.edu>).

Seismic waveforms are from IRIS Data Services (<https://www.iris.edu>), Pacific Northwest Seismic Network (<https://pnsn.org>), and INGV (Italy, <http://www.ingv.it>).

Analysis code will be deposited in a public repository on GitHub and mirrored to Zenodo with an assigned DOI upon publication.

## S9. Supplementary References

### References

- [1] C. H. Scholz, “Earthquakes and friction laws,” *Nature*, 391, 37–42 (1998).
- [2] C. Marone, “Laboratory-derived friction laws and their application to seismic faulting,” *Annu. Rev. Earth Planet. Sci.*, 26, 643–696 (1998).
- [3] J. H. Dieterich, “Time-dependent friction and the mechanics of stick-slip,” *Pure Appl. Geophys.*, 116, 790–806 (1978).
- [4] J. C. Savage and R. S. Burford, “Geodetic determination of relative plate motion in central California,” *J. Geophys. Res.*, 78, 832–845 (1973).
- [5] A. J. Haines, D. Norris, “New Zealand GPS strain rate model,” *J. Geophys. Res. Solid Earth*, 121, 2016.
- [6] L. G. Montesi and M. T. Zuber, “A unified description of stress-driven melt segregation in partially molten rocks,” *J. Geophys. Res.*, 107(B5) (2002).
- [7] M. Dragoni and A. Magnanensi, “Viscoelastic models of magma chambers,” *J. Volcanol. Geotherm. Res.*, 35, 299–314 (1988).
- [8] A. M. Jellinek and M. A. Manga, “The influence of caldera structure on magma chamber stability,” *J. Volcanol. Geotherm. Res.*, 87, 267–280 (1998).
- [9] K. Obara, “Nonvolcanic deep tremor associated with subduction in southwest Japan,” *Science*, 296, 1679–1681 (2002).
- [10] G. Rogers and H. Dragert, “Episodic tremor and slip on the Cascadia subduction zone,” *Science*, 300, 1942–1943 (2003).
- [11] M. J. Rymer et al., “The 2004 Parkfield earthquake: A case study of recurrence behavior,” *Bull. Seismol. Soc. Am.*, 96, S1–S14 (2006).

- [12] A. Ripepe and M. Chouet, “Dynamics of Strombolian eruptions,” *Geophys. Res. Lett.*, 24, 193–196 (1997).
- [13] T. H. Dixon et al., “Continuous deformation of Kilauea Volcano,” *J. Geophys. Res.*, 109, B02104 (2004).
- [14] S. C. Cohen, “Strain accumulation and release on subduction thrusts,” *Pure Appl. Geophys.*, 142, 277–291 (1994).